Quantum critical behavior of the hyperkagome magnet Mn_3CoSi

Hiroki Yamauchi,[1] Dita Puspita Sari,[2,3] Yukio Yasui,[4] Terutoshi Sakakura,[5] Hiroyuki Kimura,[6] Akiko Nakao,[7] Takashi Ohhara,[8] Takashi Honda,[9] Katsuaki Kodama,[1] Naoki Igawa,[1] Kazutaka Ikeda,[5] Kazuki Iida,[7] Daichi Ueta,[9] Tetsuya Yokoo,[9] Matthias D. Frontzek,[10] Songxue Chi,[10] Jaime A. Fernandez-Baca,[10] Kenji M. Kojima,[11] Donald Arseneau,[11] Gerald Morris,[11] Bassam Hitti,[11] Yipeng Cai,[11] Adam Berlie,[12] Isao Watanabe,[3] Pai-Tse Hsu,[13] Yu-Sheng Chen,[14] Min Kai Lee,[13] Amelia Elisabeth Hall,[15] Geetha Balakrishnan,[15] Lieh-Jeng Chang,[13,16,9,*] and Shin-ichi Shamoto[7,9,17,13,†]

[1]*Materials Sciences Research Center, Japan Atomic Energy Agency (JAEA), Tokai, Ibaraki 319-1195, Japan*
[2]*Innovative Global Program, College of Engineering, Shibaura Institute of Technology 307 Fukasaku, Minuma-ku, Saitama City, Saitama 337-8570, Japan*
[3]*Meson Science Laboratory, RIKEN Nishina Center, 2-1 Hirosawa, Wako, Saitama 351-0198, Japan*
[4]*School of Science and Technology, Meiji University, Kawasaki, Kanagawa 214-8571 27 Japan*
[5]*Neutron Industrial Technology Center, Comprehensive Research Organization for Science and Society (CROSS), Tokai, Ibaraki 319-1106, Japan*
[6]*Institute of Multidisciprinary Research for Advanced Materials, Tohoku University, Sendai 980-8577, Japan*
[7]*Neutron Science and Technology Center, Comprehensive Research Organization for Science and Society (CROSS), Tokai, Ibaraki 319-1106, Japan*
[8]*J-PARC Center, Japan Atomic Energy Agency (JAEA), Tokai, Ibaraki 319-1195, Japan*
[9]*Institute of Materials Structure Science, High Energy Accelerator Research Organization (KEK), Tsukuba, Ibaraki 305-0801, Japan*
[10]*Neutron Scattering Division, Oak Ridge National Laboratory (ORNL), Oak Ridge, Tennessee 37831, USA*
[11]*TRIUMF, Vancouver, British Columbia, V6T 2A3 Canada*
[12]*ISIS Neutron and Muon Source, Science and Technology Facilities Council, Rutherford Appleton Laboratory, Didcot OX11 0QX, United Kingdom*
[13]*Department of Physics, National Cheng Kung University, Tainan 70101, Taiwan*
[14]*National Synchrotron Radiation Research Center, Hsinchu 300092, Taiwan*
[15]*Department of Physics, University of Warwick, Coventry CV4 7AL, United Kingdom*
[16]*Institute of Physics, Academia Sinica, Taipei 115201, Taiwan*
[17]*Advanced Science Research Center, Japan Atomic Energy Agency (JAEA), Tokai, Ibaraki 319-1195, Japan*

(Received 14 September 2023; accepted 18 December 2023; published 5 February 2024)

β-Mn-type family alloys Mn_3TX (T = Co, Rh, and Ir; X = Si and Ge) have a three-dimensional antiferromagnetic (AF) corner-shared triangular network, i.e., the hyperkagome lattice. The antiferromagnet Mn_3RhSi shows magnetic short-range order over a wide temperature range of approximately 500 K above the Néel temperature T_N of 190 K. In this family of compounds, as the lattice parameter decreases, the long-range magnetic ordering temperature decreases. Mn_3CoSi has the smallest lattice parameter and the lowest T_N in the family. The quantum critical point (QCP) from AF to the quantum paramagnetic state is expected near a cubic lattice parameter of 6.15 Å. Although the Néel temperature of Mn_3CoSi is only 140 K, the emergence of the quantum critical behavior in Mn_3CoSi is discussed. We study how the magnetic short-range order appears in Mn_3CoSi by using neutron scattering, μSR, and bulk characterization such as specific heat capacity. According to the results, the neutron scattering intensity of the magnetic short-range order in Mn_3CoSi does not change much at low temperatures from that of Mn_3RhSi, although the μSR short-range order temperature of Mn_3CoSi is largely suppressed to 240 K from that of Mn_3RhSi. Correspondingly, the volume fraction of the magnetic short-range order regions, as shown by the initial asymmetry drop ratio of μSR above T_N, also becomes small. Instead, the electronic-specific heat coefficient γ of Mn_3CoSi is the largest in this Mn_3TSi system, possibly due to the low-energy spin fluctuation near the quantum critical point.

DOI: 10.1103/PhysRevResearch.6.013144

I. INTRODUCTION

Intermetallic antiferromagnet Mn_3CoSi is one of the β-Mn-type family alloys of Mn_3TX (T = Co, Rh, and

*Corresponding author: ljchang@ncku.edu.tw
†Corresponding author: s_shamoto@cross.or.jp

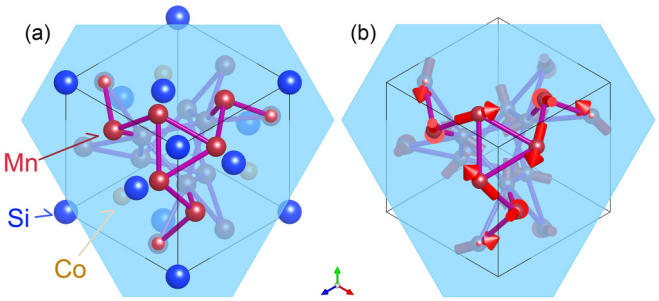

FIG. 1. Mn_3CoSi nuclear (a) and magnetic (b) structures viewed along [1, 1, 1] obtained from the structural refinements shown in this study. The red rod network is a hyperkagome lattice of Mn site (12*b*), where the Mn-Mn bond distance ranges from 2.59 to 2.64 Å. The light blue plane is (1, 1, 1). The central triangular spin cluster forms a spiral chain along [1, 1, 1].

Ir; $X =$ Si and Ge) [1–4]. They have a three-dimensional hyperkagome lattice with corner-sharing triangular Mn-spin units in a noncentrosymmetric β-Mn-type structure (Fig. 1) [5,6]. Original β-Mn is known as a spin-liquid candidate [6]. The nonmagnetic Mn sites of β-Mn can be selectively replaced by T and X elements. Non-Fermi-liquid behavior is also identified in the β-Mn, based on the exponent of the temperature dependence of the resistivity and the scaling of the dynamical spin susceptibility [7]. The family compound Mn_3RhSi shows the high-temperature short-range order (SRO) as magnetic diffuse scattering appearing up to 720 K above the Néel temperature $T_N = 190$ K, where the magnetic susceptibility deviates from the Curie-Weiss law [4]. The Weiss temperature θ_p changes from -3900 K (300–400 K) to -1500 K (720–800 K), depending on the temperature range. Based on the large Weiss temperatures, the frustration parameter, $f = |\theta_p|/T_N$, ranges from 7.9 to 20.5, suggesting spin frustration in this magnet. The large Weiss temperature also suggests large exchange interaction and large magnetic moments. The temperature dependence of the magnetic susceptibility on the Mn_3CoSi sample used for the present study deviates from the Curie-Weiss law in the paramagnetic state, too. The temperature dependence is convex above T_N [Fig. 2(b)]. These anomalous behaviors are theoretically studied as the Curie-law crossover in spin liquids, where the hyperkagome lattice is one of the largest residual entropy lattices [8]. Recently, a similar magnetic SRO has been observed in a skyrmion alloy of $Co_7Zn_7Mn_6$ with the same β-Mn crystal structure [9,10]. The Q position at ~ 1.7 Å^{-1} is identical to the observed magnetic diffuse scattering position in Mn_3CoSi, Mn_3RhSi [4], β-Mn [6], and β-$Mn_{1-x}In_x$ [11]. The magnetic short-range order originates from the local spin correlation order at low frequencies. The local spin correlation order has been observed as a cooperative paramagnetism in $Tb_2Ti_2O_7$ below 50 K [12,13]. The partial order in MnSi [14,15] and the solitonic spin liquid of $Fe_{1+y}Te$ [16] can also be categorized into the same class of the local spin correlation order in paramagnetic states.

Here we report a detailed investigation of Mn_3CoSi using probes such as neutrons and muons, complemented by specific heat capacity studies. To discuss the physical properties, they are compared with those of Mn_3RhSi and Mn_3IrSi in the Mn_3TSi phase diagram. As a result, decreasing the cubic lattice parameter, the Néel temperature, the magnetic SRO temperature, the SRO volume fraction, and the squared ordered magnetic moment decrease, suggesting a quantum critical point at $a = 6.15$ Å. On the other hand, the electronic-specific heat coefficient γ increases to the quantum critical point. These results suggest that Mn_3CoSi is the closest alloy to the quantum critical point among the Mn_3TSi alloys.

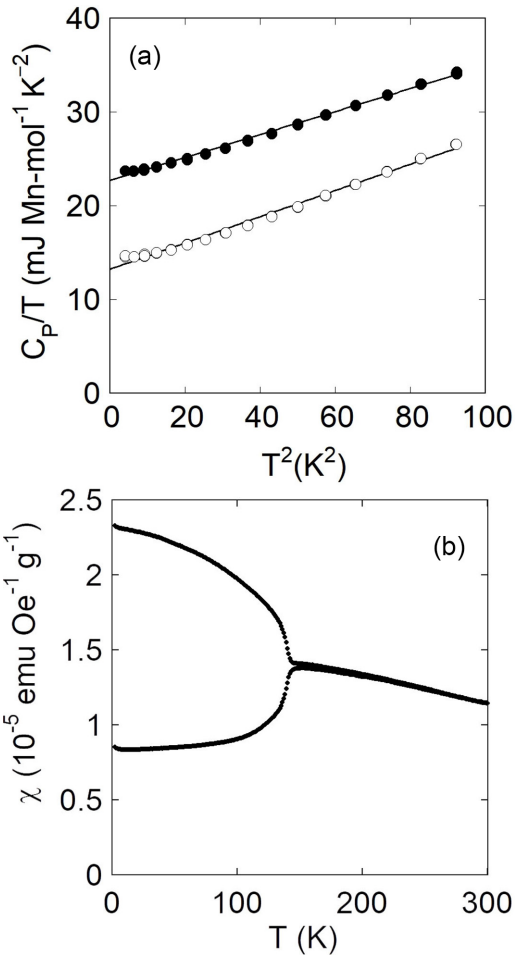

FIG. 2. Specific heat capacity and magnetic susceptibility. (a) Specific heat capacities of Mn_3CoSi (closed circles) and Mn_3RhSi (open circles) at low temperatures. The extrapolated value of C_p/T to $T^2 = 0$ by linear fitting corresponds to the electronic specific heat coefficient γ. (b) Temperature dependence of the magnetic susceptibility of Mn_3CoSi under $B \parallel [1\,1\,2] = 100$ Oe. Upper susceptibility is measured under field cooling, whereas the lower values are measured under zero-field cooling.

II. EXPERIMENTAL PROCEDURES

A. Sample preparation and the characterization

Mn_3CoSi crystals were grown by the modified Bridgman method, starting from Mn (99.9%), Co (99.9%), and Si (99.99%) placed in a commercial alumina crucible within an evacuated silica tube. The polycrystalline sample was synthesized by a conventional arc melting method in an argon atmosphere from stoichiometric amounts of powders of the

constituent elements. The as-cast ingots were sealed in an evacuated quartz tube, annealed at 1173 K for 3 days and 1073 K for 1 week, and quenched in water. The phase purity was examined by x-ray powder diffraction using a desktop diffractometer with Cu K_α radiation. No traces of impurity phases were found within the experimental accuracy. The orientations of the crystal obtained were checked using x-ray Laue diffraction. Crystal and magnetic structures were drawn by VESTA software [17]. Magnetic susceptibility and specific heat capacity measurements were carried out by Physical Property Measurement System (Quantum Design Co., Ltd.).

B. Neutron scattering measurements

The single-crystal diffraction data were taken at FONDER of JRR-3 and SENJU (BL18) of Japan Proton Accelerator Research Complex (J-PARC)/Materials and Life Science Experimental Facility (MLF) [18]. The data were analyzed using the FULLPROF and STARGAZER softwares [19,20]. The magnetic symmetry analysis was performed using the SARAh suite of programs [21]. The polycrystalline samples of Mn_3CoSi were also measured at WAND at HFIR of ORNL, HRPD at JRR-3, and NOVA(BL21) at J-PARC/MLF. Inelastic neutron scattering (INS) measurements were carried out on the chopper spectrometers POLANO (BL23) at J-PARC with a proton beam power of 600–830 kW [22]. The crystal, with a weight of about 1.6 g, was wrapped in aluminum foil and then fixed on an aluminum plate for the neutron experiment. The crystal was rotated at POLANO by 360° with a two-degree step for the rotation mode. The incident energy of POLANO was 46.27 meV under a Fermi chopper frequency of 400 Hz. The data were analyzed using the DAVE software [23]. The horizontal scattering plane of Mn_3CoSi crystal was set at POLANO by $[h, h, -h]$ and $[k, -k, 0]$ with a vertical axis of [1, 1, 2]. The polycrystal sample was measured at 4SEASONS (BL01) to observe the magnetic SRO [24,25]. The incident energy of 4SEASONS was 17.8 meV under a Fermi chopper frequency of 300 Hz. The data were analyzed using the UTSUSEMI software [26].

C. Muon spin spectroscopy measurements

The polycrystalline ingot of Mn_3CoSi was measured at ARGUS of ISIS under zero-field (ZF), longitudinal fields (LF) of 100 G and 3600 G, and a transverse field (TF) of 20 G, while the single crystal was measured at LAMPF spectrometer at M20 of TRIUMF under ZF, LF of 100 G, and TF of 25 G along [1, 1, 1].

III. RESULTS AND DISCUSSION

A. Specific heat capacity and magnetic susceptibility

The electronic specific heat coefficients γ of Mn_3CoSi and Mn_3RhSi are shown in Fig. 2(a). Mn_3CoSi γ value of 23 mJ Mn^{-1} K^{-2} is enhanced from Mn_3RhSi γ value of 12 mJ Mn^{-1} K^{-2}. Mn_3IrSi γ value is 8.8 mJ Mn^{-1} K^{-2} [27]. These results suggest that low-energy spin fluctuations coupled with conducting carriers remain without a static order. As for the β-Mn without the Néel order, the γ value is 70 mJ Mn^{-1} K^{-2}, where three magnetic moments are localized among the five Mn atoms. In other words, the enhanced γ value of Mn_3CoSi indicates the quantum critical point behavior.

As for the magnetic susceptibility, the polycrystalline samples often show magnetization anomalies above T_N. Figure 2(b) shows a small hysteresis under a small magnetic field above T_N. This is reminiscent of the Griffths phase with magnetic clusters associated with the magnetization hysteresis above T_N [28]. It may be attributed to site exchange between Mn and Co in the alloy, as the Griffiths phase can be induced even by small disorders under the competition of multiple ordered states [29]. The crystallographically high-quality single crystal of Mn_3CoSi near the quantum critical point may show the magnetic SRO above T_N, as the Griffiths phase behavior. In addition, under a small magnetic field of 100 G, weak ferromagnetic behavior is observed. Under zero-field cooling, however, antiferromagnetic (AF) behavior appears. This result is very unusual for a single-crystal magnet with little disorder. There can be two possibilities for the observed weak ferromagnetic behavior. One is the existence of weak ferromagnetic domains. The other is the creation of the magnetic domain wall with weak ferromagnetism under a magnetic field. The former is plausible because the weak ferromagnetism becomes prominent only at low magnetic fields. The ferromagnetic domains can mutually cancel out the ferromagnetic component at zero field cooling.

The origin of the ferromagnetic behavior can be the incomplete cancellation of an emergent magnetic field by scalar spin chirality [30,31], which is proposed in a kagome lattice. The kagome lattice is a two-dimensional corner-sharing network of triangle units, whereas the present hyperkagome lattice is a three-dimensional corner-sharing network of triangle units. The three-dimensional network may not cancel the emergent magnetic field. Especially, an applied magnetic field may break the cancellation of the magnetic domains with the emergent magnetic fields.

B. Neutron scattering

The magnetic diffuse scattering of Mn_3CoSi is observed as a broad signal near $Q = 1.7$ Å^{-1} at a two-axis diffractometer WAND of HFIR in ORNL [Fig. 3(a)]. However, it disappeared in the diffraction patterns at NOVA [Fig. 3(b)]. The absence of the magnetic diffuse scattering can be attributed to the energy integration difference between the two diffractometers at the continuous and pulsed neutron sources. The continuous source neutron diffractometer measures the limited Q region only in the energy integration of final energy with a constant E_i. On the other hand, the pulsed source neutron diffractometer measures both energy integrations to the incident and the final energy sides, resulting in a wider Q-range for the measurement. The absence of the magnetic diffuse scattering at NOVA also suggests that the diffuse scattering origin is the inelastic signal. As for the neutron diffraction pattern of Mn_3IrSi measured at NOVA, it does not show any magnetic diffuse scattering similar to Mn_3CoSi. The neutron diffraction pattern of Mn_3IrSi measured at ISIS also does not show the magnetic diffuse scattering [27]. They may have larger energy gaps than Mn_3RhSi in the magnetic excitation spectra. Note that the Q position of the SRO centered at ∼1.7 Å^{-1} does not coincide with any long-range magnetic Bragg peak positions.

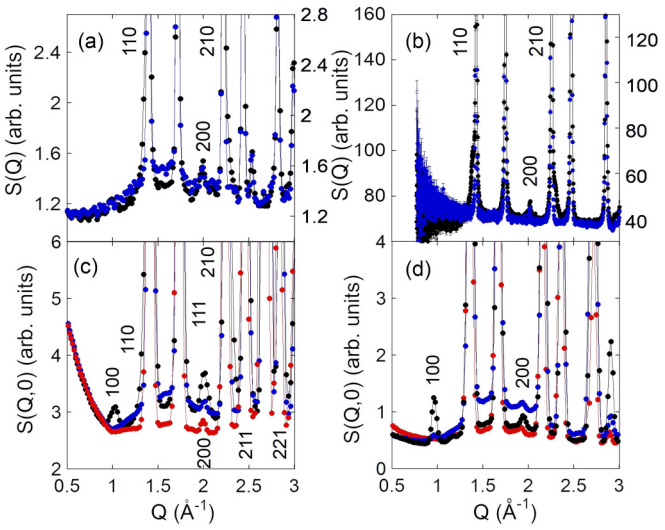

FIG. 3. Neutron scattering patterns of polycrystalline Mn_3CoSi [(a)–(c)] and Mn_3RhSi (d) samples. They are measured at WAND (a), NOVA (b), and 4SEASONS with $E_i = 18$ meV [(c), (d), Ref. [32])]. Black closed circles are measured at $T = 4$ (a), 20 (b), 7 (c), and 5 K (d). Blue closed circles are measured at $T = 200$ K [(a)–(d)]. Red closed circles are 550 K [(c) and (d)]. The intensity measured at 4SEASONS is integrated with the energy range from -1 to 10 meV. Long-range magnetic Bragg peaks such as 100 peak develop at $T =$ 5–7 K. An Al cell Bragg peak appears at $Q = 2.7$ Å^{-1}.

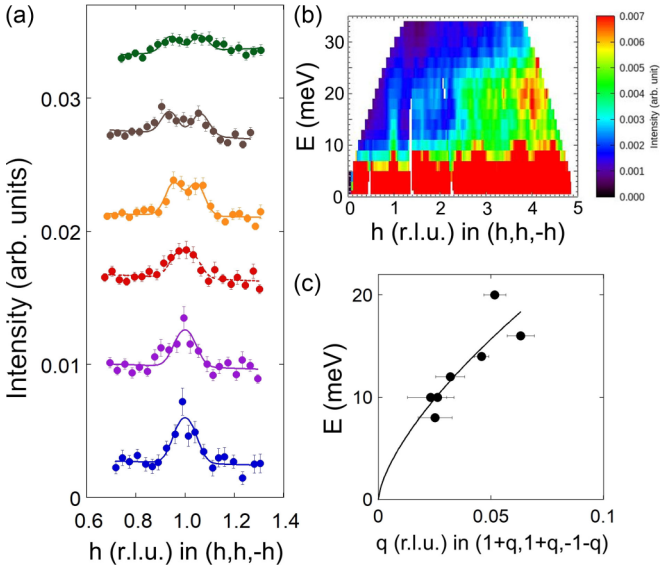

FIG. 4. Constant-E cuts of Mn_3CoSi along $[h, h, -h]$ (a). The transfer energies with an energy width of 2 meV are from 8 to 18 meV by 2 meV step from the bottom to the top. The intensity is shifted vertically. The intensity is folded for positive and negative sides. It is also integrated with the other reciprocal direction in 0.2 r.l.u. corresponding to 0.2 and 0.49 Å^{-1} for $[k, -k, 0]$ and $[\ell, \ell, 2\ell]$, respectively. The AF spin-wave dispersion can be seen at $\mathbf{Q} = (1, 1, -1)$ in the E-Q spectrum (b). The magnon dispersion fitting suggests the top energy is 55(18) meV at $q = 0.5$ (r.l.u.) (c).

The Q-position difference between SRO and long-range order (LRO) originates from the different neutron scattering configurations between the spin and the scattering vector in the elastic scattering and the inelastic scattering processes [32], suggesting that the SRO originates purely from the inelastic scattering at low energies. In other words, the elastic scattering intensity comes from $\mathbf{S}_n$ component (n denotes the normal component between the spin and the scattering vector), which does not have any structure factor at $\{1, 1, 1\}$. On the other hand, the inelastic scattering intensity has both components of $\mathbf{S}_n$ and $\mathbf{S}_p$ (p denotes the parallel component between the spin and the scattering vector), resulting in the strong magnetic signal at $\{1, 1, 1\}$, as shown in Fig. 4 [32].

In the case of Mn_3RhSi, the magnetic diffuse scattering at the two-axis diffractometer is well reproduced by integrating the energy from -1 to 10 meV [Fig. 3(d)], corresponding to the typical magnetic fluctuation energy of 10 meV [32]. So the same energy-integration is applied to the inelastic scattering patterns of Mn_3CoSi [Fig. 3(c)]. The diffraction intensity of Mn_3CoSi can be compared with that of Mn_3RhSi in an absolute scale. For example, the squared ratio of the ordered magnetic moments ($M_{Mn_3RhSi}/M_{Mn_3CoSi}$) is 2.15 at low temperatures. So, we may conclude that the observed magnetic diffuse scattering intensity is comparable for these two magnets. The magnetic diffuse scattering intensity of Mn_3CoSi remains even at 7 K, while the intensity is almost suppressed at 550 K. The results are similar to the magnetic diffuse scattering observed in β-Mn without LRO [6].

The magnetic excitation spectrum along $[h, h, -h]$ is shown in Fig. 4. The constant-E cuts at 4 K are fitted using two Gaussian peaks. The peak width was fixed to be 0.08 r.l.u. based on the fitting at $E = 14$ meV. The magnon top energy E_{top} was estimated to be 55(18) meV by a trial function $E = E_{top} \sin^{\alpha}(\pi q)$ from the fitting of Fig. 4(c), where α was 0.7(2). The dispersion top energy is higher than 39.5(6) meV of Mn_3RhSi [$\alpha = 0.53(3)$]. Based on this result, the exchange interaction may be enhanced in Mn_3CoSi compared to that of Mn_3RhSi. The magnetic excitation at $Q \sim 1.7$ Å^{-1} is extended above 140 meV in the polycrystalline sample at 4SEASONS with $E_i = 300$ meV [33], suggesting another high-energy mode above 55 meV. As for the spin-wave dispersion, we have not obtained a stable spin-wave solution to estimate the exchange parameters, possibly due to the geometrical spin frustration. The magnetic phase diagram has been studied theoretically [34,35]. However, the spin-wave dispersion with realistic exchange parameters has not been calculated for β-Mn-type alloys yet. Note that the phase diagram shows the present $q = 0$ AF state and the incommensurate AF state, which are observed experimentally [27].

Figure 5 shows the results of the single-crystal structure analysis, where 260, 252, and 40 reflections satisfying $I \geqslant 3\sigma(I)$ were used for 4 K nuclear peaks, 160 K nuclear peaks, and 4 K magnetic peaks refinements, respectively. When refining the occupancy parameters, the values were slightly above 100% [ex. the maximum occupancy was $g = 1.001(9)$ at the Co site] at all the element sites. Therefore, within the experimental accuracy, we concluded that there were no defects or substitutions of elements in the crystal structure at $T = 4$ and 160 K. In addition, the y value was 0.2029(3) in Table I, which is very close to the ideal value of 0.20346 for the perfect hyperkagome lattice with the same distance of

TABLE I. Structural parameters of Mn_3CoSi at 160 K and 4 K with the errors in the parenthesis for the corresponding digit. The space group is noncentrosymmetric $P2_13$ with a cubic lattice parameter of $a = 6.20976(5)$ Å at 4 K.

Atom	Site	x	y	z	B_{iso}(Å^2)	g
Mn	12*b*	0.1223(3)	0.2029(3)	0.4544(3)	0.59(3)	1.00(fix)
Co	4*a*	0.6856(4)	$=x$	$=x$	0.36(5)	1.00(fix)
Si	4*a*	0.0647(2)	$=x$	$=x$	0.28(3)	1.00(fix)
			$R_{F^2} = 6.63\%$, $R_F = 4.48\%$			
Atom	Site	x	y	z	B_{iso}(Å^2)	g
Mn	12*b*	0.1216(4)	0.2030(5)	0.4542(5)	0.28(3)	1.00(fix)
Co	4*a*	0.6850(7)	$=x$	$=x$	0.32(9)	1.00(fix)
Si	4*a*	0.0650(4)	$=x$	$=x$	0.21(5)	1.00(fix)
			$R_{F^2} = 6.05\%$, $R_F = 4.19\%$			
			Magnetic structural parameters of Mn_3CoSi at 4 K.			
			The magnetic structure is presented as a linear combination of three basis vectors			
			with the mixing coefficients c_i ($\sum_i c_i \Psi_i$) [21,27].			
			Magnetic moment: $m(\mathrm{Mn}) = 1.78(6)\ \mu_B$.			
			$c_1 = 0.71(3)$, $c_2 = -0.48(9)$, $c_3 = 1.55(4)$,			
			$R_{F^2} = 12.1\%$, $R_F = 8.07\%$.			

the nearest neighbor bonds between Mn [34]. In the magnetic structure analysis, the scale factor, positional parameters of the Mn atom, and extinction correlation factor were fixed at the values of nuclear structure refinement at 4 K. The magnetic Bragg peaks in the Q-range below 5 Å^{-1} were used for the refinement. In Table I, only the Mn site is a localized spin site. One may think that the Co site may also have a localized magnetic moment. First-principles calculation for Mn_3CoSi [3] reports that the Co site can have a magnetic moment of about 0.3 μ_B/Co, pointing along [1, 1, 1] directions, as shown in Fig. 5(f). Using the Mn-Co ferrimagnetic structure model, the reliability factors ($R_{F^2} = 11.6\%$, $R_F = 7.95\%$) were slightly better than those of the analysis on the Mn AF structure ($R_{F^2} = 12.1\%$, $R_F = 8.07\%$) in Table I. However, the magnetic moment of Co was 0.274(248) μ_B/Co, resulting in a small Co magnetic moment close to the analytical error. Based on the result, the magnetic moment of Co is regarded as zero here.

The obtained ordered magnetic moment at the Mn site in Mn_3CoSi was 1.78(6) μ_B, while the ordered magnetic moment of Mn_3RhSi is 2.61(3) μ_B. Compared with that of Mn_3RhSi, the magnetic moment is suppressed accompanied by the decrease of T_N from 190 to 140 K, suggesting that the Mn_3CoSi is closer to the quantum critical point. The present magnetic structure analysis at $T = 4$ K did not detect the weak ferromagnetic component, possibly because of the negligibly small component.

C. Muon spin spectroscopy

The spectra of the muon spin relaxation in zero field (ZF) and longitudinal field (LF), shown as purple and cyan data in Fig. 6(a), were analyzed using the following Kubo-Toyabe function of the asymmetry A [36].

$$A(t) = A_1 \exp(-\lambda t)\left\{\tfrac{1}{3} + \tfrac{2}{3}[1 - (\gamma_\mu \Delta)^2 t^2] \times \exp\left[-\tfrac{1}{2}(\gamma_\mu \Delta)^2 t^2\right]\right\}, \quad (1)$$

where A_1 is the initial asymmetry; γ_μ is the muon gyromagnetic ratio; Δ^2 is the second moment of the static nuclear field distribution; λ is the muon relaxation rate. In the ZF condition, at a high-temperature region above 240 K the Δ value is about 0.35 μs^{-1}. At the low-temperature region, the Δ is zero since the electronic spin is dominantly sensed by a muon. By applying a LF of 100 Oe, the nuclear field distribution is decoupled so that the Δ value is fixed to be zero for all temperature regions. Furthermore, the muon spin rotation spectra in the TF condition, shown as magenta data in Fig. 6(a), were analyzed by an exponentially damped oscillation function, as follows,

$$A(t) = A_1 \cos(B\gamma_\mu t) \exp(-\lambda t), \quad (2)$$

where B is the external applied field 25 Oe. The decreasing initial asymmetries for ZF, LF 100 Oe, and TF 25 Oe are indications of the increasing magnetic volume fraction, as plotted in Fig. 6(b). The consistency between measurement modes and samples confirm the gradual and sudden dropping in the initial asymmetry when the magnetic SRO and LRO transitions occur, respectively. In this study, we determined the SRO temperature from the TF 25 Oe measurement because of the small decrease in the asymmetry. By applying a weak TF, the spectra with almost no magnetic ordering will show an oscillation with exponential damping. Further, the oscillation component from the TF will vanish due to the development of the internal field in the fully ordered state. This distinct behavior is clearly seen in Fig. 6(a).

The initial asymmetry in Fig. 6(a) starts to decrease from $T_{SRO} = 240(10)$ K by the 6.7(23)% drop, reaching the full volume drop when LRO occurs at T_N. Meanwhile, the initial asymmetry of Mn_3RhSi starts to drop from $T_{SRO} = 720(21)$ K by 22.9% to 300 K [4]. The magnetic SRO volume fraction (SRO VF) above T_N can be attributed to the low-energy spin excitations observed by μSR remaining within the μSR energy window of 0.2 meV. As a result, the magnetic

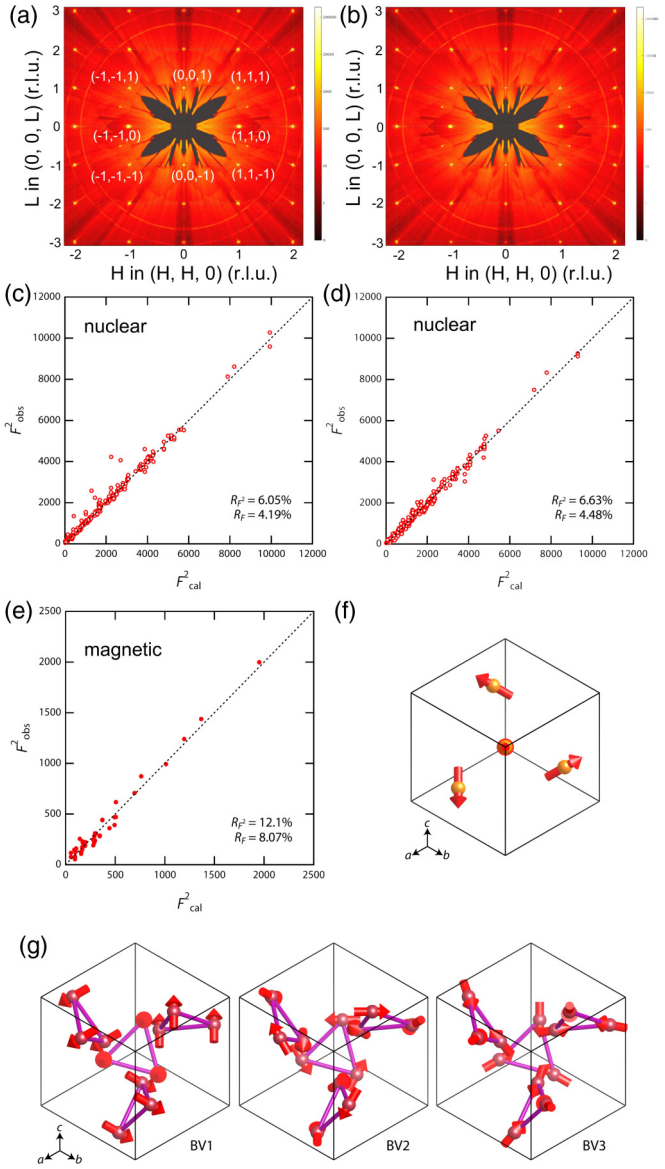

FIG. 5. Bragg peak patterns of Mn_3CoSi in the (h, h, ℓ) plane at 4 K (a) and 160 K (b). Observed nuclear Bragg peak intensities of Mn_3CoSi at 4 K (c) and 160 K (d) as a function of calculated intensities. Observed magnetic Bragg peak intensities at 4 K (e) as a function of calculated intensities. (f) Proposed magnetic structure model of the Co 4*a* site of Mn_3CoSi. (g) The obtained magnetic structure of $q = 0$ comprises three basis structures of Ψ_1(BV1), Ψ_2(BV2), and Ψ_3(BV3) [21]. Their values are listed in Table I. The refined magnetic structure is shown in Fig. 1(b).

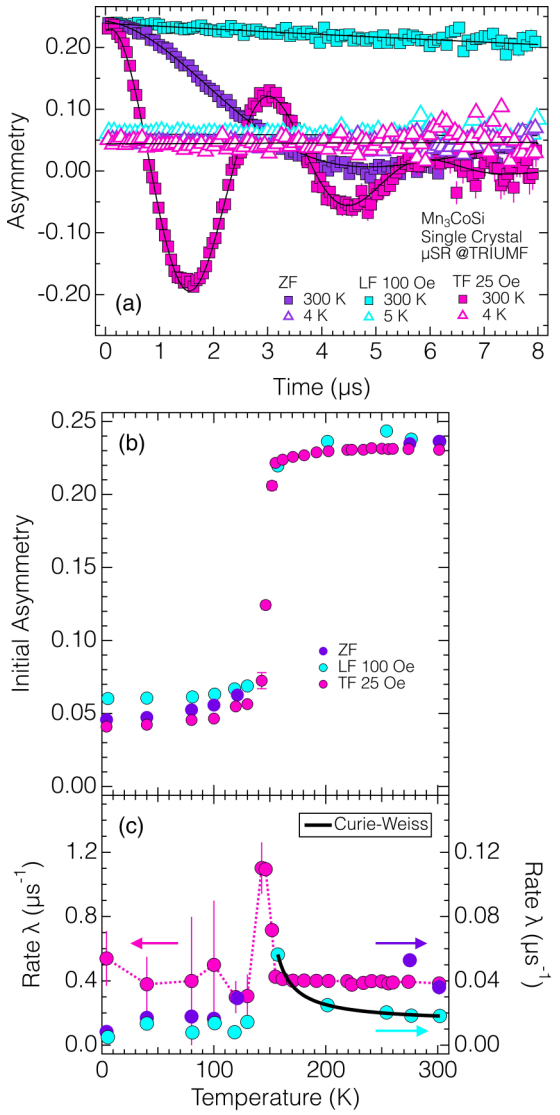

FIG. 6. (a) Time spectra of the asymmetry under zero magnetic field (ZF), longitudinal magnetic field (LF), and transverse magnetic field (TF) on Mn_3CoSi single crystal in which magnetic field is applied along [1, 1, 1]. Deduced temperature dependence of the μSR initial asymmetry (b) and the muon relaxation rate λ (c).

SRO is observed simultaneously with the initial asymmetry drop. The observed initial asymmetry drops of Mn_3CoSi and Mn_3RhSi are plotted as the VF of the magnetic SRO in Fig. 7.

The temperature dependence of the relaxation rate, λ, is plotted in Fig. 6(c). The pronounced peak indicates slowing down behavior when entering the magnetic LRO state, consistent with the sudden drop of the initial asymmetry. Thus the T_{LRO} from μSR experiment is determined at $T_{LRO} = 143$ K. Above T_{LRO}, the LF relaxation rate λ of the remaining paramagnetic component exhibits standard Curie-Weiss behavior, as shown in Fig. 6(c), where the Weiss temperature is estimated to be 142(2) K, corresponding to T_N. The same estimation had been successfully done in the case of Mn_3RhSi [4].

IV. SUMMARY

The experimental results of Mn_3TSi (T = Co, Rh, and Ir) are summarized in Fig. 7. As the cubic lattice parameter decreases, we observe that the Néel (T_N) and the magnetic short-range order (T_{SRO}) temperatures decrease to the quantum critical point which may be expected near $a = 6.15$ Å. The squared ordered magnetic moment M^2 in the long-range ordered Néel state also decreases similar to T_N. According to the simple classical mean-field theory, the effective exchange parameter J_{eff} is $\sim 3/2k_B T_N/z/M^2$, where k_B is the Boltzmann

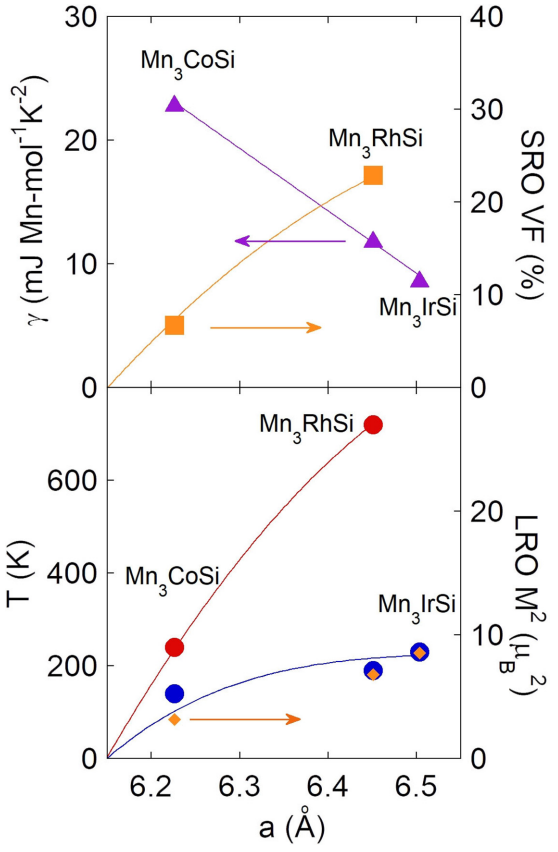

FIG. 7. Phase diagram of Mn_3TSi (T = Co, Rh, and Ir) alloys as a function of a cubic lattice parameter. The electronic specific heat coefficient γ (purple triangles) and the SRO VF (orange squares) are shown in the upper panel. The Néel temperature T_N (blue closed circles), the short-range order temperature T_{SRO} (red closed circles), and the squared long-range order magnetic moment LRO M^2 (orange diamonds) are shown in the lower panel. The Mn_3IrSi values are taken from Refs. [27,38]. The solid lines are guides to the eye.

constant, z (=6) is the number of nearest neighbor spins [37]. The effective exchange parameters J_{eff} become 11.0, 7.0, and 6.7 K for Mn_3CoSi, Mn_3RhSi, and Mn_3IrSi, respectively, suggesting that the lattice shrinkage enhances the exchange parameter. The result is consistent with the increase of E_{top} of Mn_3CoSi in comparison with that of Mn_3RhSi, although the error is comparable to the increase. The electronic specific heat coefficient γ linearly increases to the quantum critical point. This tendency is opposite to the simple bandwidth scenario, where the bandwidth should be narrow when the lattice parameter becomes large [39], which usually incurs a heavier carrier mass. So, the remanent spin fluctuation at low energy may strongly enhance the carrier mass. The hyperkagome antiferromagnet is known as one of the largest residual entropy magnets in the spin liquids [8], possibly corresponding to the large electronic specific heat coefficient γ of 70 mJ Mn mol^{-1} K^{-2} of β-Mn [6]. The magnetic volume fraction above T_N estimated by μSR above the T_N sharply decreases to the quantum critical point. All these observations point to the vicinity behavior of Mn_3CoSi to the quantum critical point.

The origin of this magnetic short-range order in a paramagnetic state is the low-energy spin fluctuation of spin clusters [32]. It may result from violating the Lifshitz condition in the noncentrosymmetric lattice with the Dzyaloshinskii-Moriya interaction [40] and the geometrical frustration of the hyperkagome lattice [4,16]. Interestingly, the spin liquid candidate, β-Mn, with non-Fermi-liquid behavior [6,7] and the skyrmion alloy $Co_7Zn_7Mn_6$ [9] with noncentrosymmetric lattices also exhibit similar magnetic short-range orders. These magnetic short-range orders may play an important role in realizing non-Fermi-liquid [7] and skyrmion states [9] by the helical spin cluster formations at low energies [32]. The Mn_3TSi alloys give us a good platform to study the anomalous metallic state with the spin cluster formation over a wide temperature range, which will be attractive for the interdisciplinary study of the role of realizing these exotic states.

ACKNOWLEDGMENTS

This work at J-PARC was performed at NOVA(BL21, 2021B0074, 2020B0415), SENJU(BL18, 2022A0263), POLANO(BL23, 2022A0202), and 4SEASONS (BL01, 2021C0001). The neutron scattering experiment at WAND of ORNL was partly supported by the U.S.-Japan Cooperative Program on Neutron Scattering under the proposals of 11391 and 13776. A portion of this research was performed using resources at the ORNL HFIR and was sponsored by the Scientific User Facilities Division, Office of Basic Energy Sciences, U.S. Department of Energy. This work at FONDER was performed by the JRR-3 general user program managed by the Institute for Solid State Physics, the University of Tokyo, under the proposal of 22812. This work at HRPD was performed by the JRR-3 general user program managed by Japan Atomic Energy Agency. The muon spin spectroscopy was performed at ARGUS of ISIS under the proposals of RB1870002 and RB2070006 and at M20 of TRIUMF under the proposal of M2201. We would like to thank Prof. T. Nakajima, Drs. S. Onoda, M. Nakamura and K. Kamazawa for valuable discussions and their help. This work was supported by Grants-in-Aid for Scientific Research (C) (No. 22K04678) from the Japan Society for the Promotion of Science. The works at National Cheng Kung University were supported by the Project NSTC 112-2112-M-006-031. The work at the University of Warwick was funded by EPSRC, UK, through Grants No. EP/N032128/1 and No. EP/T005963/1. The crystal check was performed using an X-ray Laue camera at the MLF first experiment preparation room and a magnetic properties measurement system at the CROSS user laboratory II.

[1] T. Eriksson, L. Bergqvist, P. Nordblad, O. Eriksson, and Y. Andersson, Structural and magnetic characterization of Mn_3IrGe and $Mn_3Ir(Si_{1-x}Ge_x)$: experiments and theory, J. Solid State Chem. **177**, 4058 (2004).

[2] T. Eriksson, R. Lizárraga, S. Felton, L. Bergqvist, Y. Andersson, P. Nordblad, and O. Eriksson, Crystal and magnetic structure of Mn_3IrSi, Phys. Rev. B **69**, 054422 (2004).

[3] T. Eriksson, L. Bergqvist, Y. Andersson, P. Nordblad, and O. Eriksson, Magnetic properties of selected Mn-based transition metal compounds with β-Mn structure: Experiments and theory, Phys. Rev. B **72**, 144427 (2005).

[4] H. Yamauchi, D. P. Sari, I. Watanabe, Y. Yasui, L.-J. Chang, K. Kondo, T. U. Ito, M. Ishikado, M. Hagihara, M. D. Frontzek, S. Chi, J. A. Fernandez-Baca, J. S. Lord, A. Berlie, A. Kotani, S. Mori, and S. Shamoto, High-temperature short-range order in Mn_3RhSi, Commun. Mater. **1**, 43 (2020).

[5] J. A. M. Paddison, J. R. Stewart, P. Manuel, P. Courtois, G. J. McIntyre, B. D. Rainford, and A. L. Goodwin, Emergent frustration in Co-doped β-Mn, Phys. Rev. Lett. **110**, 267207 (2013).

[6] H. Nakamura, K. Yoshimoto, M. Shiga, M. Nishi, and K. Kakurai, Strong antiferromagnetic spin fluctuations and the quantum spin-liquid state in geometrically frustrated β-Mn, and the transition to a spin-glass state caused by non-magnetic impurity, J. Phys.: Condens. Matter **9**, 4701 (1997).

[7] J. R. Stewart, B. D. Rainford, R. S. Eccleston, and R. Cywinski, Non-Fermi-liquid behavior of electron-spin fluctuations in an elemental paramagnet, Phys. Rev. Lett. **89**, 186403 (2002).

[8] R. Pohle and L. D. C. Jaubert, Curie-law crossover in spin liquids, Phys. Rev. B **108**, 024411 (2023).

[9] V. Ukleev, K. Karube, P. M. Derlet, C. N. Wang, H. Luetkens, D. Morikawa, A. Kikkawa, L. Mangin-Thro, A. R. Wildes, Y. Yamasaki, Y. Yokoyama, L. Yu, C. Piamonteze, N. Jaouen, Y. Tokunaga, H. M. Rønnow, T. Arima, Y. Tokura, Y. Taguchi, and J. S. White, Frustration-driven magnetic fluctuations as the origin of the low-temperature skyrmion phase in $Co_7Zn_7Mn_6$, npj Quantum Mater. **6**, 40 (2021).

[10] T. Nakajima, K. Karube, Y. Ishikawa, M. Yonemura, N. Reynolds, J. S. White, H. M. Rønnow, A. Kikkawa, Y. Tokunaga, Y. Taguchi, Y. Tokura, and T. Arima, Correlation between site occupancies and spin-glass transition in skyrmion host $Co_{10-x/2}Zn_{10-x/2}Mn_x$, Phys. Rev. B **100**, 064407 (2019).

[11] J. R. Stewart, A. D. Hillier, J. M. Hillier, and R. Cywinski, Structural and dynamical study of moment localization in β-$Mn_{1-x}In_x$, Phys. Rev. B **82**, 144439 (2010).

[12] J. S. Gardner, S. R. Dunsiger, B. D. Gaulin, B. D. Gingras, M. J. P. Gingras, J. E. Greedan, R. F. Kiefl, M. D. Lumsden, W. A. MacFarlane, N. P. Raju, J. E. Sonier, I. Swainson, and Z. Tun, Cooperative paramagnetism in the geometrically frustrated pyrochlore antiferromagnet $Tb_2Ti_2O_7$, Phys. Rev. Lett. **82**, 1012 (1999).

[13] J. Villain, Insulating spin glasses, Z. Phys. B **33**, 31 (1979).

[14] C. Pfleiderer, D. Reznik, L. Pintschovius, H. v. Löhneysen, M. Garst, and A. Rosch, Partial order in the non-Fermi-liquid phase of MnSi, Nature (London) **427**, 227 (2004).

[15] Y. J. Uemura, T. Goko, I. M. Gat-Malureanu, J. P. Carlo, P. L. Russo, A. T. Savici, A. Aczel, G. J. MacDougall, J. A. Rodriguez, G. M. Luke, S. R. Dunsiger, A. McCollam, J. Arai, Ch. Pfleiderer, P. Böni, K. Yoshimura, E. Baggio-Saitovitch, M. B. Fontes, J. Larrea, Y. V. Sushko, and J. Sereni, Phase separation and suppression of critical dynamics at quantum phase transitions of MnSi and $(Sr_{1-x}Ca_x)RuO_3$, Nat. Phys. **3**, 29 (2007).

[16] P. Materne, C. Koz, U. K. Rößler, M. Doerr, T. Goltz, H. H. Klauss, U. Schwarz, S. Wirth, and S. Rößler, Solitonic spin-liquid state due to the violation of the Lifshitz condition in $Fe_{1+y}Te$, Phys. Rev. Lett. **115**, 177203 (2015).

[17] K. Momma and F. Izumi, VESTA 3 for three-dimensional visualization of crystal, volumetric and morphology data, J. Appl. Cryst. **44**, 1272 (2011).

[18] T. Ohhara, R. Kiyanagi, K. Oikawa, K. Kaneko, T. Kawasaki, I. Tamura, A. Nakao, T. Hanashima, K. Munakata, T. Moyoshi, T. Kuroda, H. Kimura, T. Sakakura, C.-H. Lee, M. Takahashi, K. Ohshima, T. Kiyotani, Y. Noda, and M. Arai, SENJU: A new time-of-flight single-crystal neutron diffractometer at J-PARC, J. Appl. Cryst. **49**, 120 (2016).

[19] J. Rodríguez-Carvajal, Recent advances in magnetic structure determination by neutron powder diffraction, Phys. B: Condens. Matter **192**, 55 (1993).

[20] T. Ohhara, T. Ohhara, K. Kusaka, T. Hosoya, K. Kurihara, K. Tomoyori, N. Niimura, I. Tanaka, J. Suzuki, T. Nakatani, T. Otomo, S. Matsuoka, K. Tomita, Y. Nishimaki, T. Ajima, and S. Ryufuku, Development of data processing software for a new TOF single crystal neutron diffractometer at J-PARC, Nucl. Instrum. Methods Phys. Res. Sect. A **600**, 195 (2009).

[21] A. S. Wills, A new protocol for the determination of magnetic structures using simulated annealing and representational analysis (SARA*h*), Phys. B: Condens. Matter **276-278**, 680 (2000).

[22] T. Yokoo, K. Ohoyama, S. Itoh, J. Suzuki, K. Iwasa, T. J. Sato, H. Kira, Y. Sakaguchi, T. Ino, T. Oku, K. Tomiyasu, M. Matsuura, H. Hiraka, M. Fujita, H. Kimura, T. Sato, J. Suzuki, M. Takeda, K. Kaneko, M. Hino, and S. Muto, Newly proposed inelastic neutron spectrometer POLANO, J. Phys. Soc. Jpn. **82**, SA035 (2013).

[23] R. T. Azuah, L. R. Kneller, Y. Qiu, P. L. W. Tregenna-Piggott, C. M. Brown, J. R. D. Copley, and R. M. Dimeo, DAVE: A comprehensive software suite for the reduction, visualization, and analysis of low energy neutron spectroscopic data, J. Res. Natl. Inst. Stand. Technol. **114**, 341 (2009).

[24] R. Kajimoto, M. Nakamura, Y. Inamura, F. Mizuno, K. Nakajima, S. Ohira-Kawamura, Y. Yokoo, T Nakatani, R. Maruyama, K. Soyama, K. Shibata, K. Suzuya, S. Sato, K. Aizawa, M. Arai, S. Wakimoto, M. Ishikado, S. Shamoto, M. Fujita, H. Hiraka, K. Ohoyama, K. Yamada, and C.-H. Lee, The fermi chopper spectrometer 4SEASONS at J-PARC, J. Phys. Soc. Jpn. **80**, SB025 (2011).

[25] M. Nakamura, R. Kajimoto, Y. Inamura, F. Mizuno, M. Fujita, T. Yokoo, and M. Arai, First demonstration of novel method for inelastic neutron scattering measurement utilizing multiple incident energies, J. Phys. Soc. Jpn. **78**, 093002 (2009).

[26] Y. Inamura, T. Nakatani, J. Suzuki, and T. Otomo, Development status of software "Utsusemi" for Chopper spectrometers at MLF, J-PARC, J. Phys. Soc. Jpn. **82**, SA031 (2013).

[27] A. E. Hall, P. Manuel, D. D. Khalyavin, F. Orlandi, D. A. Mayoh, L.-J. Chang, Y.-S. Chen, D. G. C. Jonas, M. R. Lees, and G. Balakrishnan, Comparative study of the magnetism in Mn_3RhGe and related compound Mn_3IrSi, Phys. Rev. Mater. **7**, 114402 (2023).

[28] R. B. Griffiths, Nonanalytic behavior above the critical point in a random Ising ferromagnet, Phys. Rev. Lett. **23**, 17 (1969).

[29] J. Burgy, M. Mayr, V. Martin-Mayor, A. Moreo, and E. Dagotto, Colossal effects in transition metal oxides caused by intrinsic inhomogeneities, Phys. Rev. Lett. **87**, 277202 (2001).

[30] H. Ishizuka and N. Nagaosa, Spin chirality induced skew scattering and anomalous Hall effect in chiral magnets, Sci. Adv. **4**, eaap9962 (2018).

[31] N. Nagaosa, Emergent electromagnetism in condensed matter, Proc. Jpn. Acad., Ser. B **95**, 278 (2019).

[32] S. Shamoto, H. Yamauchi, K. Iida, K. Ikeuchi, A. E. Halle, Y.-S. Chen, M. K. Lee, G. Balakrishnan, and L.-J. Chang, Spiral spin cluster in the hyperkagome antiferromagnet Mn_3RhSi, Commun. Phys. **6**, 248 (2023).

[33] S. Shamoto, H. Yamauchi, K. Iida, K. Ikeuchi, H. Saito, T. Nakajima, Y.-S. Chen, S. Yano, P. T. Hsu, M. K. Lee, A. E. Hall, G. Balakrishnan, and L.-J. Chang, Magnetic excitation in the hyperkagome antiferromagnet Mn_3RhSi (unpublished).

[34] B. Canals and C. Lacroix, Mean-field study of the disordered ground state in the β-Mn lattice, Phys. Rev. B **61**, 11251 (2000).

[35] H.-K. Jin and Y. Zhou, Classical and quantum order in hyperkagome antiferromagnets, Phys. Rev. B **101**, 054408 (2020).

[36] R. Kubo and T. Toyabe, *Magnetic Resonance and Relaxation*, edited by R. Bline (North-Holland, Amsterdam, 1966).

[37] W. Jones and N. H. March, *Theoretical Solid State Physics, Volume 1: Perfect Lattices in Equilibrium* (Dover, New York, 1985), p. 367.

[38] Y. Ōnuki, Y. Kaneko, D. Aoki, A. Nakamura, T. D. Matsuda, M. Nakashima, Y. Haga, and T. Takeuchi, Single Crystal Growth and Magnetic Properties of Noncentrosymmetric Antiferromagnet Mn_3IrSi, J. Phys. Soc. Jpn. **91**, 065002 (2022).

[39] W. A. Harrison, *Electronic Structure and the Properties of Solids: The Physics of the Chemical Bond* (Dover, New York, 1989).

[40] I. E. Dzyaloshinskii, Theory of helicoidal structures in antiferromagnets. I. nonmetals, Sov. Phys. JETP **19**, 960 (1964).